Earth and Planetary Science Letters 303 (2011) 59–70

Contents lists available at ScienceDirect

Earth and Planetary Science Letters

journal homepage: www.elsevier.com/locate/epsl

Are diamond-bearing Cretaceous kimberlites related to low-angle subduction beneath western North America?

Claire A. Currie [a,*], Christopher Beaumont [b]

[a] Department of Physics, University of Alberta, Edmonton AB, Canada
[b] Department of Oceanography, Dalhousie University, Halifax, NS, Canada

ARTICLE INFO

Article history:
Received 17 September 2010
Received in revised form 3 December 2010
Accepted 18 December 2010
Available online 26 January 2011

Editor: R.D. van der Hilst

Keywords:
kimberlite
subduction
Farallon plate
laramide orogeny
continental lithosphere

ABSTRACT

Diamond-bearing Cretaceous kimberlites of western North America were emplaced 1000–1500 km inboard of the Farallon plate subduction margin and overlap with the development of the Western Interior Seaway, shut-down of the Sierra Nevada arc, and the Laramide orogeny. These events are consistent with a decrease in subduction angle along much of the margin, which placed the subducted Farallon plate in close proximity to the continental interior at the time of kimberlite magmatism. Our numerical models demonstrate that low-angle subduction can result from high plate convergence velocities and enhanced westward motion of North America. Further, rapid subduction allows hydrous minerals to remain stable within the cool interior of the subducting plate to more than 1200 km from the trench. Destabilization of these minerals provides a fluid source that can infiltrate the overlying material, potentially triggering partial melting and kimberlite/lamproite magmatism.

1. Introduction

Kimberlites, and to a lesser extent lamproites, are the main host materials for economic diamond deposits. In cool cratonic lithosphere, diamonds form at depths greater than 140 km and are transported rapidly to the surface through entrainment by kimberlite and lamproite magmas. The origin of this magmatism and its interaction with cratonic lithosphere is therefore the key to understanding the emplacement of diamond-bearing kimberlites.

Kimberlites (used here to include lamproites when appropriate) generally occur in continental interiors far from plate margins, making their relationship to plate tectonic processes enigmatic. Proposed models for kimberlite genesis include mantle plumes (e.g., Crough et al., 1980), continental extension (e.g., Phipps, 1988) and melts originating in the mantle transition zone or deeper (e.g., Ringwood et al., 1992; Torsvik et al., 2010). An alternative mechanism, potentially applicable to a limited subset of kimberlite events, invokes a relationship between kimberlite magmatism and lithospheric subduction, in which fluids released by prograde metamorphism of the subducting plate trigger partial melting of the overlying material to form kimberlite magma (Helmstaedt and Gurney, 1997; McCandless, 1999).

The latter mechanism has been used to relate Cretaceous kimberlites of the Western Interior of North America to Farallon plate subduction (McCandless, 1999; McCandless and Tosdal, 2005). These kimberlites were emplaced in a kimberlite corridor (KC) along the western edge of the Proterozoic and Archean basement comprising cratonic North America (Fig. 1), 1000–1500 km inboard of, and parallel to, the Cretaceous subduction margin. The main emplacement phase occurred from ca. 105 to ca. 45 Ma (Heaman et al., 2003), primarily in the Late Cretaceous, followed by sporadic lamproites and related volcanics in the western U.S. (Table 1). It is significant that kimberlite locations within KC do not correspond to known mantle plume hotspot tracks (Heaman et al., 2003) and specifically lie outside regions of upwelling from the deep mantle (Torsvik et al., 2010).

The later stages of KC magmatism temporally overlap with the Laramide orogeny (ca. 80–50 Ma), which produced widespread deformation of western North America. This orogeny has been attributed to a decrease in Farallon subduction angle and associated enhanced mechanical coupling along the plate interface (e.g., Bird, 1988; Dickinson and Snyder, 1978). Shallow angle subduction may have also produced extensive hydration of the western North American lithosphere (e.g., Humphreys et al., 2003).

In this study, we investigate the subduction hypothesis for KC kimberlites by: 1) presenting evidence that the Farallon plate was suitably positioned beneath North America as early as 100 Ma, 2) developing a numerical model of low-angle subduction, and 3) using the model to assess the potential for subduction-related

* Corresponding author. Department of Physics, University of Alberta, 11322-89 Avenue, Edmonton, AB, T6G 2G7, Canada. Tel.: +1 780 492 1062; fax: +1 780 492 0714.
E-mail address: claire.currie@ualberta.ca (C.A. Currie).

0012-821X/$ – see front matter © 2010 Elsevier B.V. All rights reserved.
doi:10.1016/j.epsl.2010.12.036

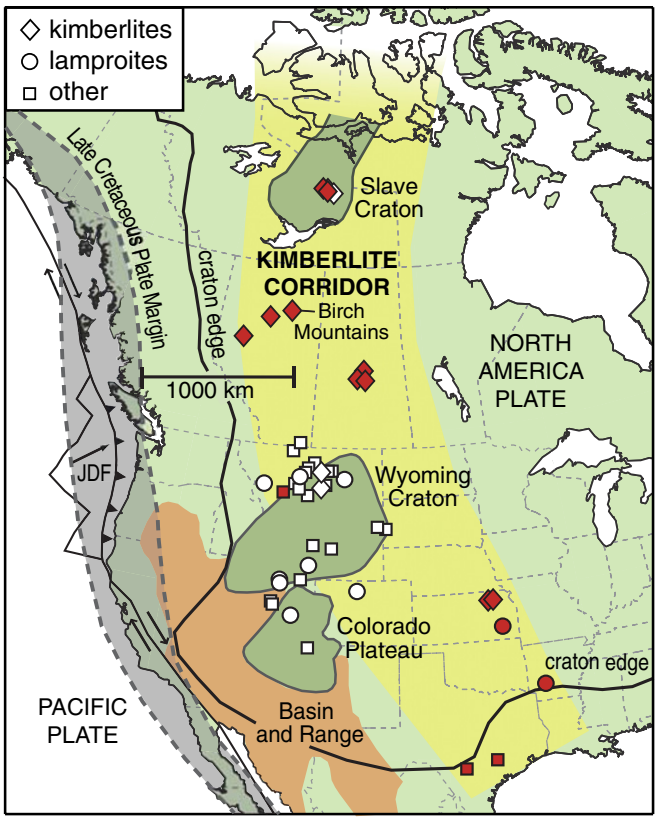

Fig. 1. Distribution of kimberlites, lamproites and related volcanics (ages in Table 1). Red symbols indicate Cretaceous emplacement ages; open symbols are Cenozoic ages. Shaded grey region shows the range in position of the Late Cretaceous plate margin. The Juan de Fuca plate (JDF) is the remaining fragment of the Farallon plate. The Birch Mountains kimberlites are the most northern site that may be related to low-angle Farallon plate subduction. Further work is needed to assess a subduction source for the Slave Craton kimberlites.

volatiles in kimberlite magma genesis. We focus on Cretaceous and early Cenozoic kimberlites; later (<45 Ma) kimberlites coincide with widespread volcanism in the western U.S. that has been linked with rapid removal of the low-angle Farallon plate (Humphreys et al., 2003).

2. Farallon plate geometry inferred from dynamical subsidence of the Western Interior

We first consider the evolving position of the Farallon plate beneath North America. Dynamical subsidence of the Earth's surface provides a proxy for the reconstruction of subducting plate geometry (e.g., Mitrovica et al., 1989). Mantle flow associated with subduction induces a dynamic load on the overlying continent, and the spatial wavelength of the resulting surface subsidence is related to the dip of the subducting plate; long wavelengths reflect low-angle subduction.

For western North America, sedimentation records document the Cretaceous development of the Western Interior Seaway (WIS) through westward tilting of the continent (e.g., Cross and Pilger, 1978; DeCelles, 2004; Smith et al., 1994) (Fig. 2). Initial Aptian (~120 Ma) marine inundation formed an elongate north–south seaway opening to the Arctic Ocean. This connected to the Gulf of Mexico later in the Albian (~105 Ma), and at its widest, the WIS expanded as far east as the present-day Lake Superior. The seaway persisted, with the last record of marine sedimentation at the end of the Cretaceous. The width of the WIS, which spans the KC, is too large to have been solely foreland flexure caused by orogenic loading (e.g., Liu and Nummedal, 2004). The WIS was already wide as early as the Albian (Fig. 2). Such broad subsidence over wavelengths of ~1500 km requires dynamical loading attributable to low-angle or flat-slab subduction of the Farallon plate (Burgess et al., 1997; Mitrovica et al., 1989).

This conclusion is supported by inverse mantle convection models that calculate the planform dynamical subsidence of North America since 100 Ma (Liu et al., 2008; Spasojevic et al., 2009) based on backward calculation (retrodiction) of the trajectory of the Farallon plate from its current location below eastern North America (e.g., Bunge and Grand, 2000; Sigloch et al., 2008). Despite uncertainties in variables such as eustatic sea level, this analysis confirms a wide region of low-angle Farallon plate subduction below much of western North America. By 100 Ma, low-angle subduction was in place as far north as ~60° N. This evolved into a limited region of flat slab subduction in the western United States starting at ~90 Ma, fringed by a 1000 km wide area of low-angle subduction to the north and east. Specifically, "at 100 Ma the slab [was] shallow dipping but not flat lying. Slab flattening [started] at about 90 Ma" (Liu et al., 2008). This reconstruction places the Farallon plate beneath the westward-drifting North American plate at the time of KC magmatism.

The WIS subsidence observations indicate an earlier onset of low-angle subduction that affected a wider region than previously inferred from studies of Laramide tectonics (e.g., Dickinson and Snyder, 1978). Conventional interpretations cite cessation of Sierra Nevada arc magmatism at ~80 Ma and subsequent eastward migration of magmatism as indicators of shallowing subduction below the southwestern U.S. part of the Farallon plate margin (e.g., Coney and Reynolds, 1977), implying normal subduction before this time. The Campanian (80 Ma) arc shut-down lags the minimum Cenomanian age inferred for the onset of dynamical subsidence (Liu and Nummedal, 2004; Liu et al., 2008; Spasojevic et al., 2009) by 20 Ma.

The subsidence data provide evidence that dynamical loading affected a region well inboard of the Sierran arc, an indicator of shallow angle subduction, whereas the persistence of arc magmatism indicates the presence of a mantle wedge until 80 Ma. However, neither observation allows the plate position to be reconstructed accurately. This dichotomy could, for example, be resolved if, at ~100 Ma, the dip of the Farallon plate was steep enough near the subduction zone to allow the hot mantle wedge to persist and arc magmatism to continue, but the dip decreased to the east, thereby causing dynamical subsidence. This proposed geometry would also be consistent with westward motion of North America as the Atlantic opened, such that the Farallon plate was overridden by North America at a rate that exceeded its sinking velocity. Only later, at the onset of the Laramide orogeny, did the near-trench subduction geometry become shallow. With the final removal of hot mantle wedge in this area, the Sierran Arc was extinguished and Laramide-style deformation initiated through enhanced mechanical coupling with the Farallon plate. Although this proposed evolution cannot be tested, we conclude that there is evidence that there was an early onset of low angle subduction, sufficient that it should not be dismissed.

3. Testing the subduction hypothesis for kimberlites

We employ two-dimensional, plane-strain dynamical numerical models to examine the development of low-angle subduction and test the "Farallon hydration" hypothesis for the overlying North American lithosphere (Humphreys et al., 2003). Our goal is to study the first order characteristics of low-angle subduction in a situation that is analogous to western North America but without details that are specific to this case. The model parameterization is therefore purposefully parsimonious. For example, we use a simplified structure for the oceanic and continental lithospheres and the plate velocities specified at the model boundaries are constant with time. Furthermore, the model domain is a two-dimensional vertical cross-section, which allows for a detailed examination of across-

Table 1
Cretaceous to recent kimberlites, lamproites and related volcanics.

State/province	Volcanic field	Type	Age (Ma)	Reference
Kimberlites and lamproites				
NWT	Ekati	Kimberlite	75–45	Heaman et al. (2004)
	Diavik	Kimberlite	56–55	Heaman et al. (2004)
	Hardy Lake	Kimberlite	73–71	Heaman et al. (2004)
AB	Mountain Lake	Kimberlite	79–72	Heaman et al., 2004; Eccles et al., 2004
		Kimberlite	68	Heaman et al. (2004)
	Birch Mountains	Kimberlite	79–70	Heaman et al. (2004)
	Buffalo Head Hills	Kimberlite	99–92	Eccles et al. (2008)
		Kimberlite	88–86	Heaman et al. (2004)
SK	Fort a la Corne	Kimberlite	104–101	Heaman et al. (2004)
		Kimberlite	95	Heaman et al. (2004)
	Sturgeon Lake	Kimberlite	98 ± 1	Heaman et al. (2004)
	Candle Lake	Kimberlite	?	
MT	Highwood Mountains	Lamproite	54–50	Irving and Hearn (2003)
	Homestead	Kimberlite	51–50	Irving and Hearn (2003)
	Bear Gulch	Lamproite	49–48	Irving and Hearn (2003)
	Williams	Kimberlite	48 ± 2.5	Heaman et al. (2004)
	Smoky Butte	Lamproite	27.6	Irving and Hearn (2003)
WY	Leucite Hills	Lamproite	3.0–0.89	Irving and Hearn (2003)
CO	Middle Park	Lamproite	33 ± 0.8	Thompson et al. (1997)
UT	Francis	Lamproite	35–41	Wannamaker et al., 2000; Irving and Hearn, 2003
	Robbers Roost	Lamproite	22	Wannamaker et al. (2000)
	White's Creek	Lamproite	13.9	Irving and Hearn (2003)
KS	Stockdale	Kimberlite	112 ± 6	Heaman et al. (2004)
	Leonardville/Bala	Kimberlite	104 ± 4	Griffin et al. (2004)
	Winkler	Kimberlite	95 ± 6	Heaman et al. (2004)
	Ross Dome	Lamproite	91–88	Cullers et al. (1996)
AR	Prairie Creek	Lamproite	106 ± 3	Griffin et al. (2004)
Related volcanics				
AB	Milk River	Minette	52–49	Buhlmann et al. (2000)
MT	Elkhorn Mountains	Lamprophyre	78–73	Irving and Hearn (2003)
	Little Belt Mountains	Minette	58–44	Irving and Hearn (2003)
	Bearpaw Mountains	Minette	54–50	O'Brien et al., 1995; Irving and Hearn, 2003
	Sweetgrass Hills	Minette	54–50	O'Brien et al., 1995; Irving and Hearn, 2003
	Crazy Mountains	Minette	53–48	O'Brien et al., 1995; Irving and Hearn, 2003
	Zortman dike	Alnöite	52	Irving and Hearn (2003)
	Castle Mountains	Minette	52–47	Irving and Hearn (2003)
	Eagle Buttes	Minette	52–50	O'Brien et al., 1995; Irving and Hearn, 2003
	Ricker Butte	Alnöite	51	Irving and Hearn (2003)
	Winnett Sill	Alnöite	50	O'Brien et al. (1995)
	Porcupine Dome	Carbonatite	~50	Irving and Hearn (2003)
	Black Hills–Bear Lodge Mountains	Minette/carbonatite	50–48	Irving and Hearn (2003)
	Haystack Butte	Melnoite	47.9	Irving and Hearn (2003)
WY	Cedar Mountain	Lamprophyre	~35	Irving and Hearn (2003)
	Sage Creek	Minette	22.2	Irving and Hearn (2003)
UT	Mona	Lamprophyre	23	Wannamaker et al. (2000)
	Wasatch Plateau	Lamprophyre	24–7	Wannamaker et al. (2000)
AZ/UT/CO/NM	Navajo province	Lamprophyre	28–19	Wannamaker et al. (2000)
TX	Balcones Province	Nephelinite	84–76	Phipps (1988); Griffin et al. (2009)

margin structure but cannot provide information on the planform variation of the North American and Farallon plates.

3.1. Model geometry

The initial model geometry is shown in Fig. 3. The continental plate is divided into two regions to represent the general structure of western North America: (1) "Phanerozoic" lithosphere adjacent to the plate margin with a total thickness of 120 km, and (2) inboard "craton" lithosphere of 200 km total thickness. The 90 km thick oceanic lithosphere is consistent with a >100 Ma Farallon plate age (Engebretson et al., 1984). Previous studies have suggested that subduction of thickened oceanic crust played a key role in the development of low-angle subduction below North America and the Laramide orogeny (Liu et al., 2010; Livacarri et al., 1981; Saleeby, 2003). As demonstrated below, subduction of a thick oceanic plateau is not required for low-angle subduction and therefore we have not included it in the model, but later we note its possible contribution to dehydration reactions.

Plate convergence is imposed through assigned boundary velocities, and subduction initiation is aided by a zone of rheologically weak material (seed) at the boundary between the oceanic and continental plates. This material is subducted with the oceanic plate and does not affect subsequent model behavior. After subduction initiation, the model evolves dynamically in response to boundary velocities and internal buoyancy forces.

3.2. Governing equations

The thermal–mechanical evolution of the system is calculated assuming plane strain, incompressibility, and zero Reynolds number. Material deformation is governed by the equations of (1) conservation of volume when incompressible (and mass when compressible during metamorphic phase changes) and (2) force balance:

$$\frac{\partial v_j}{\partial x_j} = 0 \tag{1}$$

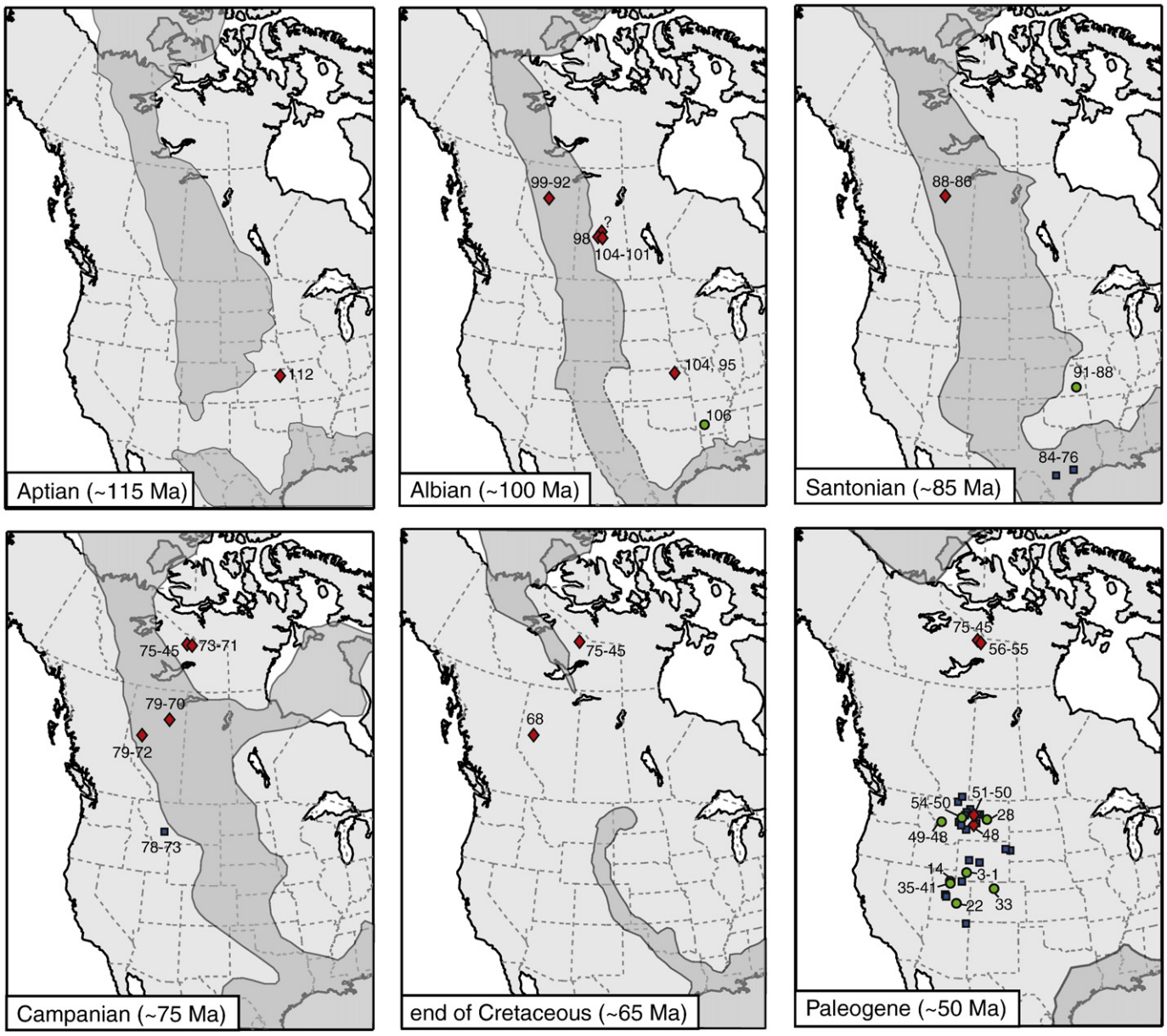

Fig. 2. Distribution of the Western Interior Seaway based on Smith et al. (1994) and the paleogeography maps of Ron Blakey, NAU Geology (http://jan.ucc.nau.edu/~rcb7/nam.html). Also shown are the locations of kimberlites (diamonds), lamproites (circles), and related volcanics (squares) emplaced during the same time interval (ages in Ma). Present-day geography is shown for reference; this has not been corrected for Cretaceous and Cenozoic deformation.

$$\frac{\partial \sigma_{ij}}{\partial x_i} + \rho g = 0 \quad i,j = 1,2 \tag{2}$$

where $x_{i,j}$ are spatial coordinates, v_i and v_j are components of velocity, ρ is density, and g is (vertical) gravitational acceleration. Repeated indices imply summation. The associated stress tensor is:

$$\sigma_{ij} = -P\delta_{ij} + \sigma'_{ij} = -P\delta_{ij} + 2\eta_{eff}\dot{\varepsilon}_{ij} \tag{3}$$

where P is pressure (mean stress), σ'_{ij} is the deviatoric stress tensor, η_{eff} is effective viscosity, δ_{ij} is the Kronecker delta (1 for i = j and 0 otherwise), and the strain rate tensor is:

$$\dot{\varepsilon}_{ij} = \frac{1}{2}\left(\frac{\partial v_i}{\partial x_j} + \frac{\partial v_j}{\partial x_i}\right) \tag{4}$$

The temperature field is calculated using the energy balance equation:

$$\rho c_p\left(\frac{\partial T_K}{\partial t} + v_i\frac{\partial T_K}{\partial x_i}\right) = k\frac{\partial}{\partial x_i}\frac{\partial T_K}{\partial x_i} + A + \sigma'_{ij}\dot{\varepsilon}_{ij} + v_2\alpha g T_K \rho \tag{5}$$

where c_p is specific heat, T_K is the absolute temperature, t is time, k is thermal conductivity, A is volumetric radioactive heat production, and α is the volumetric thermal expansion coefficient. The last two terms on the right-hand side correspond to strain heating, assuming all dissipated mechanical energy is converted to heat (term 3), and the temperature correction for adiabatic heating for vertical velocity v_2 (term 4). The thermal field is coupled to the mechanical field through the strain heating term, redistribution of radioactive heat-producing materials by material flow, and the temperature-dependent density and viscous rheology of model materials.

These equations are solved, subject to specified boundary conditions, using Arbitrary Lagrangian–Eulerian finite element techniques (Fullsack,

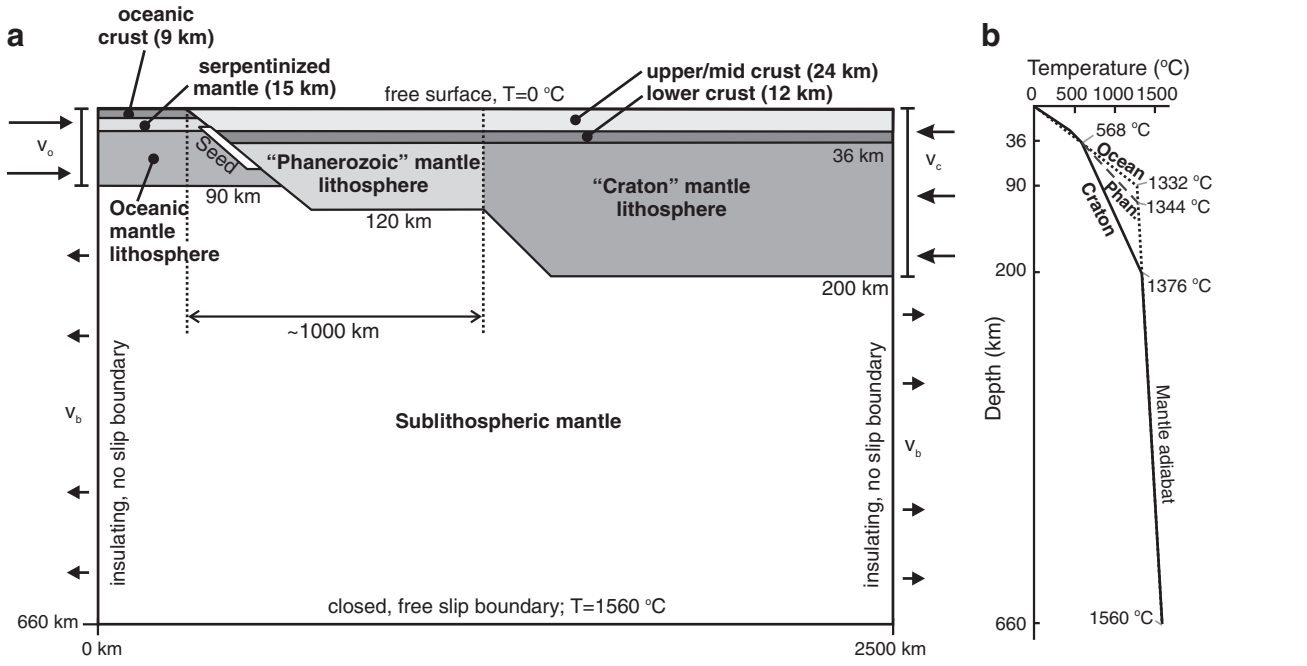

Fig. 3. a) Initial geometry of the numerical models. The thermal and mechanical boundary conditions are indicated. Prescribed influx velocities for the oceanic plate (V_o) and continental plate (V_c) are balanced by a uniform outflux velocity (V_b) along the side boundaries of the sublithospheric mantle. b) Oceanic and continental craton geotherms prescribed to incoming lithosphere at the left and right boundaries of the models, respectively. The average geotherm for the Phanerozoic (Phan.) continental lithosphere at the start of the model is also shown.

1995). Mechanical and thermal calculations are carried out on a Eulerian grid that stretches vertically to conform to the upper model surface. The Eulerian grid has 250 elements in the horizontal direction (10 km width) and 108 elements in the vertical direction, with 60 elements in the upper 180 km (3 km height) and 48 elements below (10 km height). Materials are tracked on a Lagrangian mesh and additional Lagrangian tracer particles that are advected with the model velocity field and are used to update the Eulerian model material distribution.

3.3. Material properties

All materials have a viscous-plastic rheology. At deviatoric stress below frictional-plastic yield, deformation is viscous, with an effective viscosity (η_{eff}^{v}) given by:

$$\eta_{eff}^{v} = \frac{f}{W_S}\left(B^*\right)\left(\dot{I}_2'\right)^{(1-n)/n}\exp\left(\frac{Q + PV^*}{nRT_K}\right) \quad (6)$$

where f is a scaling factor, W_S is the strain-weakening factor, $\dot{I}_2'$ is the square root of the second invariant of the strain rate tensor ($\dot{I}_2'^2 = \frac{1}{2}\dot{\varepsilon}_{ij}\dot{\varepsilon}_{ij}$), R is the gas constant (8.3145 J mol^{-1} K^{-1}), and B*, n, Q and V* are the pre-exponential viscosity parameter, stress exponent, activation energy and activation volume from laboratory data. The parameter B* includes a conversion from the uniaxial laboratory experiments to the tensor invariant state of stress used in the models.

The scaling factor (f) allows the effective viscosity to be scaled upward or downward to approximate strength variations owing to changes in composition or volatile content relative to laboratory samples. This also allows an investigation of model sensitivity to variations in effective viscosity associated with uncertainties in the laboratory-derived parameters (Beaumont et al., 2006). Furthermore, all materials undergo viscous strain weakening ($W_S = 25$) over an accumulated strain (I_2') of 2 to 5, consistent with values used in previous studies (e.g., Warren et al., 2008). Such viscous strain weakening represents a combination of as yet poorly constrained effects, including reaction weakening, grain size reductions, and the effects of weakening by infiltrating hydrous and other fluids.

Frictional-plastic deformation is defined by a Drucker–Prager yield criterion:

$$J_2' = P\,sin\phi_{eff} + c_0 \quad (7)$$

where J_2' is the square root of the second invariant of the deviatoric stress tensor ($J_2'^2 = \frac{1}{2}\sigma_{ij}'\sigma_{ij}'$), c_0 is the cohesion, and ϕ_{eff} is the effective internal angle of friction, which includes the effects of pore fluid pressure according to $P\sin\phi_{eff} = P(1-\lambda)\sin\phi$, where λ is the pore fluid pressure ratio and ϕ is the dry coefficient of internal friction. Plastic deformation is modeled by defining an effective viscosity that places the state of stress on yield (Fullsack, 1995; Willett, 1999). All materials undergo frictional-plastic strain softening through a decrease in ϕ_{eff} from 30° to 2° over accumulated strain (I_2') of 0.5 to 1.5, as an approximation of material softening or an increase in pore fluid pressure with increasing strain (Beaumont et al., 2006; Huismans and Beaumont, 2003).

Table 2 gives the properties for the model materials. Viscous rheologies used in the current models follow those of earlier studies (Beaumont et al., 2006; Currie et al., 2008; Warren et al., 2008). Mantle materials have a viscous rheology based on the wet olivine flow law of Karato and Wu (1993). A scaling factor ($f = 10$) is applied to all oceanic and continental mantle lithosphere to approximate strengthening resulting from dehydration and melt depletion during lithosphere formation. The oceanic crust and lower continental crust follow the Mackwell et al. (1998) flow law for dry Maryland diabase (with $f = 0.1$), and the upper-mid continental crust has a viscous rheology based on wet quartzite (Gleason and Tullis, 1995) (with $f = 5$).

All materials have a thermal conductivity of 2.25 W m^{-1} K^{-1} below 1344 °C (i.e., within the lithosphere), which linearly increases to 52 W m^{-1} K^{-1} at 1376 °C. The high conductivity in the sublithospheric mantle corresponds to scaling the thermal conductivity by the Nusselt number of upper mantle convection. This maintains a nearly constant basal temperature for the lithosphere and an adiabatic temperature

Table 2
Material parameters used in the numerical models.

	Cont. upper–mid crust	Cont. lower crust	Oceanic crust	Cont. and oceanic mantle lithosphere	Sublithospheric mantle
Plastic rheology					
c_0 (MPa)	2	0	0	0	0
ϕ_{eff}	30° to 2°	30° to 2°	30° to 2°	30° to 2°	30° to 2°
Viscous rheology					
f	5	0.1	0.1	10	1
W_S	25	25	25	25	–
A ($Pa^{-n}\ s^{-1}$)	1.10×10^{-28}	5.05×10^{-28}	5.05×10^{-28}	3.91×10^{-15}	3.91×10^{-15}
B* ($Pa\ s^{1/n}$)[a]	2.92×10^{6}	1.91×10^{5}	1.91×10^{5}	1.92×10^{4}	1.92×10^{4}
N	4.0	4.7	4.7	3.0	3.0
Q ($kJ\ mol^{-1}$)	223	485	485	430	430
V* ($cm^3 mol^{-1}$)	0	0	0	10	10
Thermal parameters					
k ($W\ m^{-1}\ K^{-1}$)[b]	2.25	2.25	2.25	2.25	2.25
A ($\mu W\ m^{-3}$)	1.15	0.55	0	0	0
c_p ($J\ kg^{-1}\ K^{-1}$)	750	750	750	1250	1250
Density [c]					
ρ_0 ($kg\ m^{-3}$)	2800	2900	2950	3250	3250
T_0 (°C)	200	500	0	1344	1344
Eclogite ρ_0 ($kg\ m^{-3}$)	–	–	3300	–	
Eclogite T_0 (°C)			500		
α (K^{-1})	3.0×10^{-5}	3.0×10^{-5}	3.0×10^{-5}	3.0×10^{-5}	3.0×10^{-5}

[a] $B^* = (2^{(1-n)/n}3^{-(n+1)/2n})A^{-1/n}$. The term in brackets converts the pre-exponential viscosity parameter from uniaxial laboratory experiments (A) to the tensor invariant state of stress of the numerical models.
[b] Thermal conductivity at temperatures less than 1344 °C; at higher temperatures, thermal conductivity increases linearly from 2.25 W $m^{-1}\ K^{-1}$ at 1344 °C to 52.0 W $m^{-1}\ K^{-1}$ at 1376 °C.
[c] Density varies with temperature: $\rho(T) = \rho_0[1-\alpha(T-T_0)]$, where ρ_0 is the reference density at temperature T_0 and α is the volumetric thermal expansion coefficient.

gradient in the sublithospheric mantle, without the need to explicitly model upper mantle convection (Pysklywec and Beaumont, 2004). Numerical models that use a constant thermal conductivity of 2.25 W $m^{-1}\ K^{-1}$ for all materials exhibit a similar evolution to those shown below, but undergo enhanced secular cooling.

3.4. Boundary conditions and initial thermal structure

Thermal and mechanical boundary conditions are shown in Fig. 3. Plate convergence is imposed through assigned velocities for the oceanic (V_o) and continental (V_c) lithosphere at the side boundaries of the model. Mass balance is maintained using a uniform outflux through the side boundaries of the sublithospheric mantle. The models are solved in the continental reference frame by adding velocity V_c to all side boundaries. Temperatures of the oceanic and continental craton lithosphere at the model boundaries are given by conductive geotherms (Fig. 3b). The oceanic geotherm is consistent with that of an oceanic plate older than 100 Ma (Stein and Stein, 1992). The continental craton geotherm is calculated using a surface heat flow of 55 mW/m^2, the thermal properties of continental crustal materials (Table 2) and a thermal conductivity of 4.22 W $m^{-1}\ K^{-1}$ for the mantle lithosphere, such that the conductive geotherm intersects a 1296 °C mantle adiabat at 200 km depth (i.e., the base of the craton lithosphere).

The initial 2D steady-state thermal structure of the model domain is calculated using the assigned thermal boundary conditions and material thermal properties. In this calculation, the craton mantle lithosphere has a thermal conductivity of 4.22 W $m^{-1}\ K^{-1}$ so that its starting thermal structure is consistent with the 200 km thick lithosphere. The models also undergo internally-induced isostatic adjustment prior to subduction initiation that produces variations in initial surface elevation owing to lateral variations in material and thermal densities.

4. Model results

Various factors have been proposed for triggering the Late Cretaceous shallowing of the Farallon plate, including enhanced convergence rates and an increase in North America westward velocity (Engebretson et al., 1984), subduction of thickened oceanic crust (Livacarri et al., 1981; Saleeby, 2003), and interactions between the subducting plate and the thick continental craton lithosphere (e.g., O'Driscoll et al. 2009). Here, we investigate the role of plate velocities, in particular the known rapid subduction of the Farallon plate and the westward velocity of North America. The current lower mantle position of seismic velocity anomalies, interpreted as Farallon plate remnants, is consistent with 16–18° of westward displacement of the North America plate relative to the deep mantle since the Early Cretaceous (van der Meer et al., 2010). In the model below, constant velocities of 11 cm/yr eastward and 4 cm/yr westward are used for the oceanic and continental plates, respectively, comparable to the inferred average Cretaceous–Cenozoic plate velocities (Engebretson et al., 1984).

Fig. 4a shows this model at 20 Ma-emt (elapsed model time, i.e., the time after subduction initiation in the model). At this point, a well-developed subduction zone has been established. With continued rapid plate convergence, the subducting plate trajectory becomes shallower (Fig. 4b). As the oceanic plate encounters the craton, the lowermost craton lithosphere is entrained by the slab (Fig. 4c). At 76 Ma-emt, the subducting plate is in contact with continental lithosphere at 100–150 km depth to >1500 km from the trench (Fig. 4d).

This geometry is consistent with isotopic data from Cenozoic mafic volcanics which indicates that continental mantle lithosphere remained below much of the western U.S. during the Laramide orogeny (Livaccari and Perry, 1993) and with P-T data from Oligocene eclogite xenoliths from the Colorado Plateau (~700 km from the trench), interpreted as Farallon plate crust (Usui et al., 2003). In the model, low-angle subduction results in progressive cooling of the continental lithosphere, in agreement with thermochronologic data for the western U.S. (Dimitru et al., 1991). Our time-dependent model has a hotter continental lithosphere than predicted by existing thermal-kinematic models (e.g., Bird, 1988; English et al., 2003) which, as noted by Lee (2005), are cold owing to thermal steady state and the absence of an asthenospheric mantle wedge.

In the above model, low-angle subduction develops in response to the applied plate velocities, especially continental plate motion. When

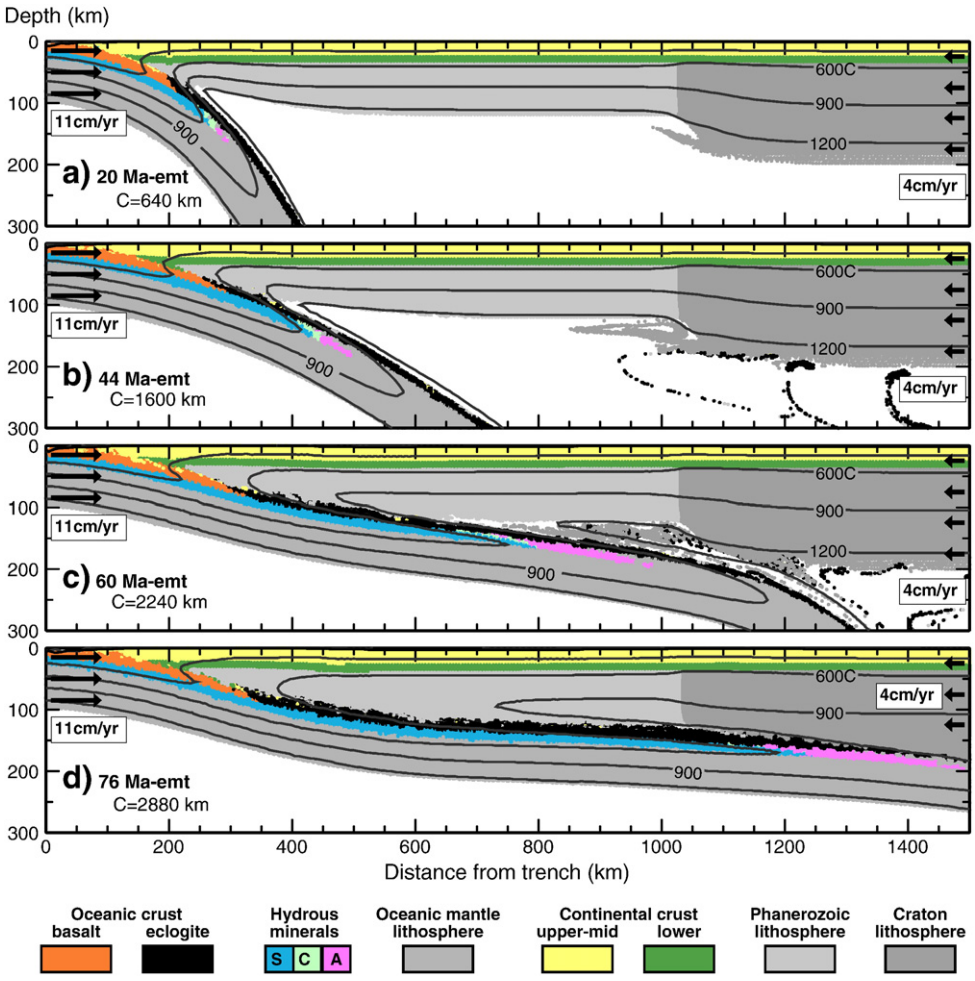

Fig. 4. Numerical model at: a) 20 Ma-emt, b) 44 Ma-emt, c) 60 Ma-emt, and d) 76 Ma-emt, where emt is the elapsed model time (the time after subduction initiation in the models). Models are shown in the continental reference frame; C is the distance that the continent has overridden the subduction zone. Hydrous minerals are serpentinized mantle (antigorite, S), chlorite (C), and 10 Å phase (A).

viewed in the fixed subduction zone reference frame, the continent advances at 4 cm/yr and overrides the subduction zone, resulting in a low-angle subduction regime even with the old, dense oceanic plate. We also tested a model in which the continental plate is stationary and the oceanic plate velocity is 15 cm/yr, giving the same 15 cm/yr convergence velocity. All other parameters are identical to the above model. In this case, the subducting plate maintains a steep trajectory throughout its 60 Ma evolution and does not flatten below the continental plate (Fig. 5). These results are consistent with those of van Hunen et al. (2004) which indicate that continental overthrusting is the main factor controlling the development of low-angle subduction.

5. Hydrous minerals within the Farallon plate and implications for metasomatism

5.1. Fluid sources

The subduction hypothesis (McCandless, 1999) links kimberlite magma genesis with volatiles released from the subducting oceanic plate. We focus on slab dehydration, as the addition of H_2O-rich fluids to the overlying mantle will decrease its solidus temperature, promoting partial melting and magma generation (e.g., Katz et al., 2003; Schmidt and Poli, 2003). Elsewhere, we consider slab decarbonation and melting. The transport and release of H_2O from the low-angle slab is assessed by mapping the stability of hydrous phases in oceanic crust and mantle in the model described above. Dehydration of subducted sediments and continental crust likely yield only small volumes of H_2O (Hacker, 2008).

Oceanic plate dehydration occurs continuously with increasing pressure and temperature (Schmidt and Poli, 2003). As oceanic crust is largely anhydrous once in the eclogite stability field, we monitor the location of the basalt–eclogite transition in the oceanic crust, using the phase diagram for mid-oceanic ridge basalt (Hacker et al., 2003) and assuming no kinetic delay in the phase transition. As oceanic crust enters the eclogite stability field in the model, its density is increased, representing complete transformation to eclogite facies rocks (Hacker, 1996). The phase change only affects the density; thermal and rheological parameters are not changed.

Serpentinization of the uppermost oceanic mantle may result from water introduced by faulting prior to subduction (e.g., Hacker, 2008; Schmidt and Poli, 2003). We assume a 15 km thick serpentinized layer and monitor the stability of serpentine (antigorite), chlorite and 10 Å phase, using the phase diagram for H_2O-saturated peridotite of Schmidt and Poli (2003) (Fig. 6). Material properties do not change as oceanic mantle lithosphere passes through the different stability fields.

The distribution of hydrous phases for the low-angle subduction model is shown in Figs. 4 and 6. The old oceanic plate remains cool as it is rapidly subducted. During early steep subduction, dehydration of the model oceanic crust and serpentinized mantle occurs beneath the putative volcanic arc (70–140 km depth). As the subduction trajectory shallows, the location of the slab dehydration shifts landward. This effect is enhanced as the slab comes into contact with continental lithosphere, pinching out the hot mantle wedge. At 76 Ma-emt, the

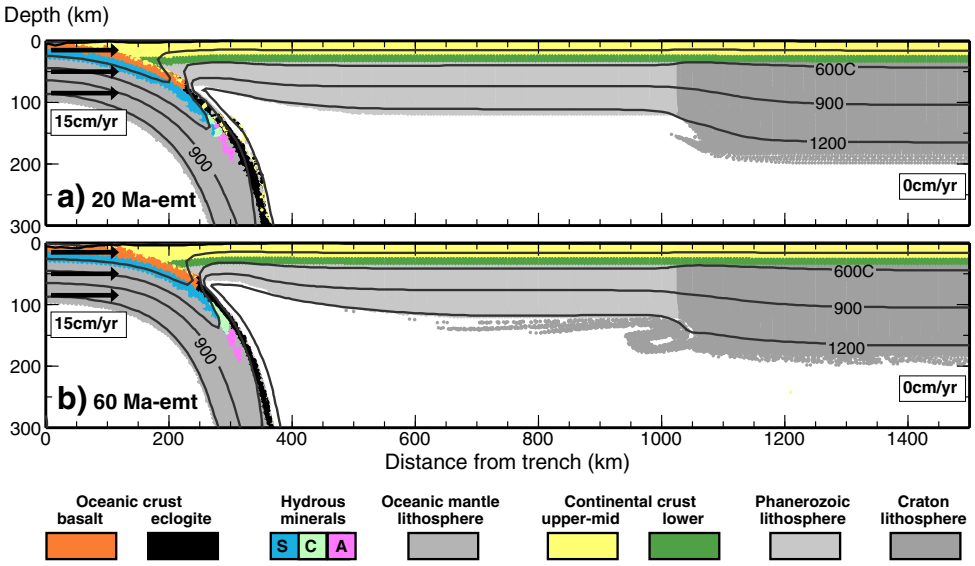

Fig. 5. Numerical model with a stationary over-riding plate at: a) 20 Ma-emt and b) 60 Ma-emt. Hydrous minerals are serpentinized mantle (antigorite, S), chlorite (C) and 10 Å phase (A).

basalt–eclogite transition for oceanic crust occurs 300–350 km from the trench. Serpentinized peridotite remains stable to over 1200 km from the trench, and dehydration occurs over an additional 300 km, as material passes through 10 Å phase before becoming anhydrous. In contrast, for the steep-angle subduction model, dehydration of the oceanic crust and serpentinized mantle lithosphere occurs within 350 km of the trench, well seaward of the cratonic continental lithosphere (Fig. 5).

Subduction of thickened oceanic crust (e.g., a plateau) along the same low-angle trajectory is expected to have a similar dehydration pattern to that shown in Fig. 4. The basalt–eclogite transition may occur slightly further inboard, owing to the longer time needed to heat the thicker crust. The thicker crust will also delay the heating of the underlying mantle lithosphere and therefore dehydration of this layer would be shifted inboard by a small amount. Numerical models of van Hunen et al. (2002) indicate that the location of oceanic crust eclogitization is similar for models with and without an oceanic plateau.

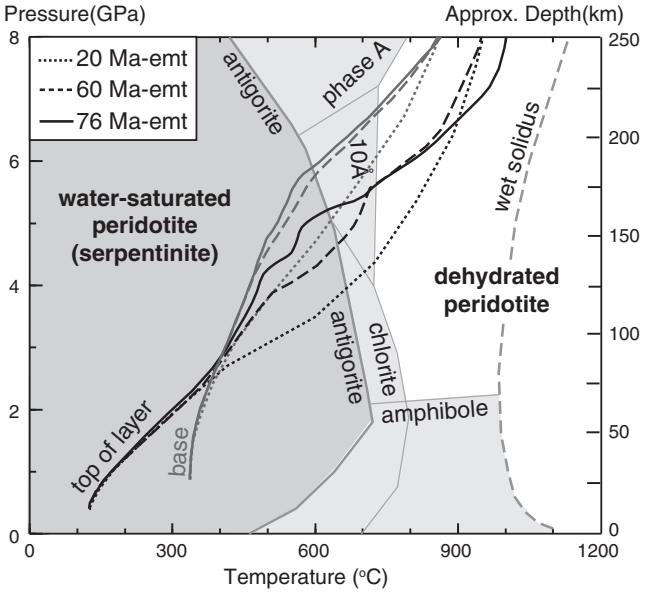

Fig. 6. Pressure–temperature plots for top and bottom of serpentinized oceanic mantle lithosphere layer at different elapsed model times (emt) for the low-angle subduction model shown in Fig. 4. Phase diagram for hydrated peridotite from Schmidt and Poli (2003).

Transport of hydrous fluids from the subducted oceanic plate to the overlying material is not explicitly modeled, but it is expected that transport occurs rapidly along subvertical paths corresponding to the direction of the maximum fluid pressure gradient (e.g., Cagnioncle et al., 2007; Elliott, 2003). In particular, if the subducting plate is in close proximity to the continental lithosphere (e.g., Fig. 4c and d), metasomatism of the continental lithosphere is expected to occur in the region that is above the point of volatile release from the oceanic plate.

Our results confirm the Humphreys et al. (2003) hypothesis that low-angle Farallon plate subduction may have hydrated the North America continental lithosphere to >1000 km from the plate margin. This is consistent with mantle xenoliths in the Cenozoic volcanics that indicate hydrated lithosphere across much of the western U.S. (e.g., Dixon et al., 2004 and references therein; Li et al., 2008; Smith et al., 2004; Smith, 2010). Isotopic and trace element data support a subduction source for the fluids (e.g., Facer et al., 2009; Lee, 2005; Perkins et al., 2006; Rowe and Lassiter, 2009), and fluid addition is inferred to have occurred since 100 Ma (e.g., Carlson et al., 2004; Mirnejad and Bell, 2006; O'Brien et al., 1995; Smith and Griffin, 2005).

5.2. Fluid sinks

Hydration of the craton lithosphere by fluids derived from the underlying low-angle slab may trigger partial melting, owing to the decrease of the solidus temperature by H_2O addition. We map the area of potential melting using the parameterization of the hydrous peridotite solidus given by Katz et al. (2003). At each point in the craton lithosphere, we calculate the amount of water (in bulk wt.%) that would be needed to induce melting at the in-situ pressure–temperature conditions (Fig. 7). The region of potential melting is bounded by the water-saturated solidus (Fig. 6), and within this region, only a small amount of H_2O (0.2–0.3 bulk wt.%) is needed to stabilize the melt. Here, we assume no previous hydration melting of this type. That is, we assume the cratonic lithosphere is initially 'dry' and therefore has not undergone earlier melting because its temperature is well below the anhydrous peridotite solidus (Katz et al., 2003). In nature, there may have been previous metasomatic events that induced melting (e.g., Griffin et al., 2004).

As the subducting plate trajectory shallows in the models, the craton lithosphere is cooled and the potential melt region migrates landward. During cooling, the area that is susceptible to melting is situated above and horizontally overlaps the location of dehydration of the oceanic plate, supporting the idea that some parts of the deep craton may undergo

partial melting during the development of low-angle subduction. Cooling of the lithosphere by prolonged low-angle subduction should prohibit further melting, although slab dehydration may continue, producing a hydrated continental lithosphere that is prone to widespread melting triggered by heating associated with later removal of the low-angle slab (c.f. Humphreys et al., 2003).

6. Discussion and conclusions

Kimberlite and lamproite magmas are small volume, potassic, volatile-rich ultramafic melts that originate within or below the diamond stability field (Mitchell, 1986). The hybrid nature of these magmas makes it difficult to infer the primary source (Becker and Le Roex, 2006). A key constraint comes from Hf–Nd systematics showing that these magmas plot below the mantle array, hence requiring a source component that has been isolated from convecting mantle for >1 Ga (Nowell et al., 2004). One interpretation invokes melting of ancient oceanic material in the mantle transition zone or deeper (e.g., Nowell et al., 2004; Ringwood et al., 1992). Others place the source in the deep continental mantle lithosphere and attribute the negative εHf–εNd signature to melting of either chemically distinct veins (e.g. Choukroun et al., 2005; Griffin et al., 2000), or a thin, compositionally distinct layer at the base of the lithosphere (e.g., Bell and Moore, 2004). Kimberlite models with a continental lithosphere source propose a two-stage process to explain the geochemical and isotopic characteristics (e.g., Choukroun et al., 2005; Le Roex et al., 2003; Malkovets et al., 2007): (1) an ancient metasomatic event that introduced volatiles into the deep, previously depleted, continental lithosphere through channelized flow, creating veins of modified mantle lithosphere and (2) a more recent event that triggered partial melting of the deep lithosphere; the latter is the process that we are investigating.

As argued above, the continental-scale Western Interior Seaway was significantly wider than predicted for flexural orogenic loading and is more consistent with dynamic subsidence associated with an extensive region of low-angle subduction. This placed the Farallon plate below, and likely in close proximity to, cratonic lithosphere at the time of KC magmatism. The Farallon plate would have screened the continent from material rising from greater depths, making models of a deep mantle origin for these particular kimberlites problematic unless the magma passed through slab tears or holes. It is also unlikely that kimberlite magmatism reflects melting of the Farallon plate; kimberlite compositions are inconsistent with melting of recently subducted material (Nowell et al., 2004), and our numerical model shows the oceanic mantle lithosphere is too cool

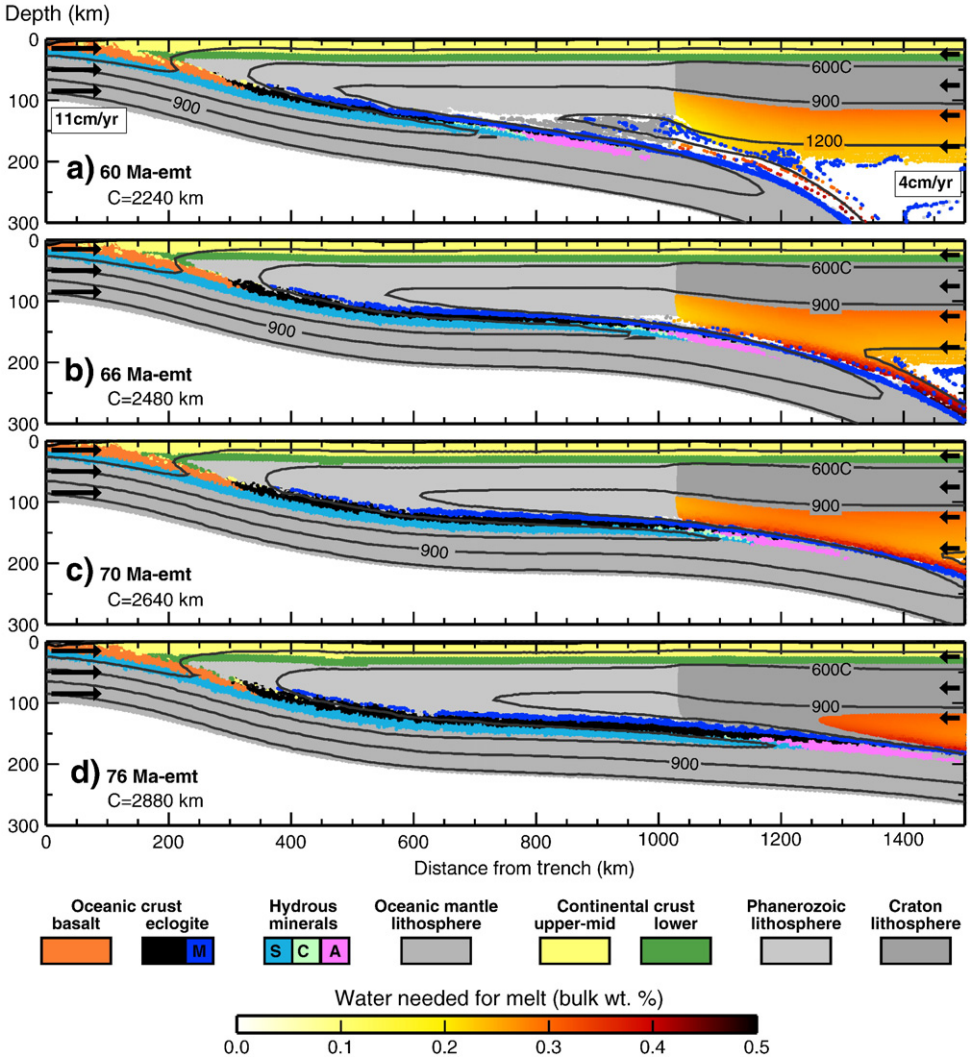

Fig. 7. Assessment of the link between slab dehydration and craton lithosphere melting during low-angle subduction at: a) 60 Ma-emt, b) 66 Ma-emt, c) 70 Ma-emt, and d) 76 Ma-emt. Orange-red region in the craton mantle lithosphere shows the material that may undergo hydrous melting; the scale bar shows the amount of water (bulk wt.%) needed to induce melting at the pressure–temperature conditions within this region. Dark blue particles (M) indicate oceanic crust or subducted sediments that are at temperatures above their wet solidus. Hydrous minerals are serpentinized mantle (antigorite, S), chlorite (C) and 10 Å phase (A).

to melt (Fig. 6). Modeled oceanic crust temperatures are, however, above the basalt wet solidus during low angle subduction (Fig. 7). Although this material is dehydrated, melting could be induced through H_2O infiltration from the underlying lithospheric mantle (i.e., flush melting, Schmidt and Poli, 2003). Limited oceanic crust melting may explain xenolith trace element data from the Colorado Plateau that suggest continental lithosphere metasomatism by both an aqueous fluid and silicate melt (Lee, 2005). The wet solidus for pelitic sediments is comparable to that of MORB (Schmidt and Poli, 2003), and therefore subducted sediments on top of the oceanic crust may also undergo flush melting.

Our preferred model places the source region of KC magmas above the low-angle Farallon plate and directly implicates Farallon plate devolatilization in magma genesis (Fig. 8). The numerical models demonstrate that, owing to its old age and rapid subduction rate, hydrous minerals could have been preserved in the Farallon plate to 1000–1500 km from the trench. As these minerals destabilized below the western North American craton, hydrous fluids were released into the overlying lithosphere, or the region immediately below it. We propose that the influx of fluids triggered a small amount of partial melting of the deep craton lithosphere, forming the source for kimberlite and lamproite magmas. The sporadic nature of KC magmatism may reflect variability in the degree of Farallon plate dehydration and factors controlling magma transport and extrusion (e.g., lithosphere structure and far-field plate stresses).

The kimberlite magma source in this model represents a mixture between components derived from both the subducting plate and deep craton mantle lithosphere. Geochemical studies demonstrate that kimberlite compositions are consistent with low degree (~1%) melting of refractory, metasomatically enriched, continental mantle (Becker and Le Roex, 2006; Le Roex et al., 2003), including veins or isolated regions of mantle lithosphere that were metasomatized before 1 Ga and therefore contain a negative εHf–εNd signature (Griffin et al., 2000). In addition, both H_2O and CO_2 are required in the kimberlite source region (e.g., Le Roex et al., 2003; Mitchell, 1986 and references therein). In our model, H_2O is derived directly from slab dehydration and is the key factor that induces melting. The subducting plate may also be the source of CO_2. In particular, melting of carbonated oceanic crust and sediments provides an effective means of transferring CO_2 to the overlying material (e.g., Kerrick and Connolly, 2001; Thomsen and Schmidt, 2008). A sediment contribution is in accord with kimberlite compositions that indicate a source with a high K_2O/Na_2O ratio (e.g., Mirnejad and Bell, 2006).

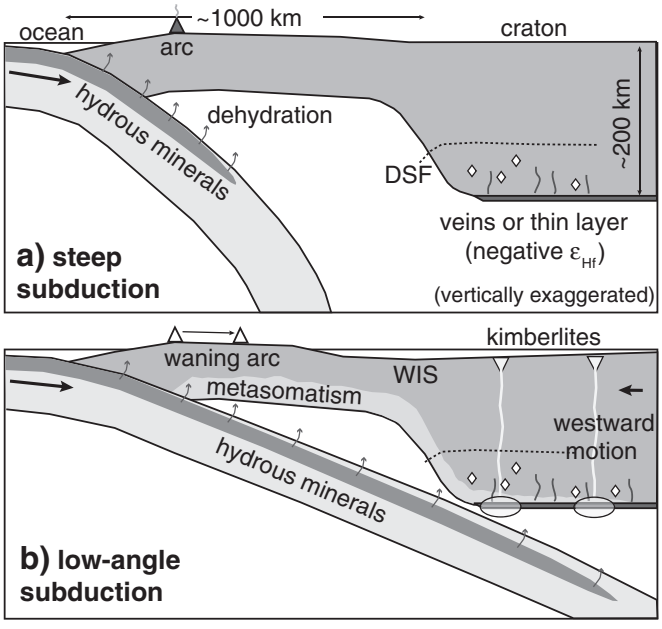

Fig. 8. Inferred relationship between Farallon plate subduction and kimberlite magmatism. a) Early Cretaceous geometry with steep-slab subduction. DSF = diamond stability field. b) Late Cretaceous shallowing of the Farallon plate allowed hydrous minerals to be transported >1200 km inboard where destabilization resulted in metasomatism of the overlying material and kimberlite magmatism. WIS = Western Interior Seaway.

This model is consistent with geochemical analyses of Cenozoic lamproites of the Wyoming craton that indicate a lithospheric source region that was subject to recent (<100 Ma) metasomatism (Mirnejad and Bell, 2006). Furthermore, these rocks indicate a complex geochemical evolution of the western U.S. lithosphere prior to 100 Ma, including early melt depletion followed by a Proterozoic metasomatic event (>1 Ga) (Downes et al., 2004; Mirnejad and Bell, 2006; O'Brien et al., 1995). The kimberlites themselves remain more enigmatic, and further work is needed to assess the presence of a subduction component in the magma source region. For example, oxygen isotope data indicate no strong subduction signature in several KC kimberlites (Schulze et al., 2001). However, a subduction component is not generally observed in oxygen isotopes from volcanic arc magmas (Eiler et al., 2000) where it would be more likely. We are not aware of other studies that have examined KC kimberlites and lamproites for a subduction component.

In conclusion, our study supports a causal link between Farallon plate subduction and Cretaceous KC magmas. At the time of magmatism, the Farallon plate was suitably positioned, and numerical models demonstrate the development of low-angle subduction and transport of hydrous minerals beneath the KC, where slab dehydration is consistent with kimberlite and lamproite magma generation in the cratonic lithosphere above. The subsidence history of the Western Interior Seaway indicates low-angle subduction along much of the plate margin to ~60° N (Liu et al., 2008). Therefore, the proposed model may be valid for the Late Cretaceous Birch Mountains kimberlites and regions to the south, but further work is needed to extend this model north to the Slave Craton kimberlites (Fig. 1).

Rapid, low-angle subduction reaching beneath cratonic continental interiors appears to be relatively rare, and therefore, subduction-related magmatism may be limited to only a small number of kimberlite events. Other mechanisms are likely responsible for kimberlites where there is no evidence for contemporaneous low-angle subduction. Examples where there is a spatial–temporal correlation between kimberlites and subduction include the Devonian kimberlites of the Wyoming Craton (Carlson et al., 2004), Carboniferous and Triassic diamonds of eastern Australia, and Mesozoic kimberlites of South Africa (McCandless, 1999). In the case of eastern Australia, the Copeton and Bingara alluvial type B diamonds are anomalous and may have been derived directly from the subducting plate during the formation of the New England fold belt (Davies et al., 2002, 2003; Sutherland and Barron, 2003). However, because they are alluvial, it is not known how they were transported to the surface. A potential modern analogue is the central Chile flat slab region which projects under the Rio de la Plata craton. This region contains Mesozoic deep-seated volcanics (Comin-Chiaramonti et al., 2010), so it will be necessary to distinguish any modern occurrences from the pre-existing population.

Acknowledgements

We thank Thomas Stachel, Yana Fedortchouk and Larry Heaman for helpful discussions, and Dan Schulze for comments on oxygen isotopes. Gene Humphreys, Sandra Wyld, and three anonymous reviewers provided constructive comments, and we thank Rob van der Hilst for his editorial handling of this manuscript. Numerical modeling software was developed by Phillippe Fullsack (Dalhousie University). Research support provided by NSERC and an IBM Shared University Research (SUR) grant.

References

Beaumont, C., Nguyen, M., Jamieson, R., Ellis, S., 2006. Crustal flow modes in large hot orogens. In: Law, R.D., Searle, M.P., Godin, L. (Eds.), Crustal Flow, Ductile Extrusion and Exhumation in Continental Collision Zones: Geol. Soc. Spec. Publ., vol. 268, pp. 91–145.

Becker, M., Le Roex, A.P., 2006. Geochemistry of South African on- and off-craton, group I and group II kimberlites: petrogenesis and source region evolution. J. Petrol. 47, 673–703.

Bell, D.R., Moore, R.O., 2004. Deep chemical structure of the southern African mantle from kimberlite megacrysts. S. Afr. J. Geol. 107, 59–80.

Bird, P., 1988. Formation of the Rocky Mountains, western United States: a continuum computer model. Science 239, 1501–1507.

Buhlmann, A.L., Cavell, P., Burwash, R.A., Creaser, R.A., Luth, R.W., 2000. Minette bodies and cognate mica-clinopyroxenite xenoliths from the Milk River area, southern Alberta: records of a complex history of the northernmost part of the Archean Wyoming craton. Can. J. Earth. Sci. 37, 1629–1650.

Bunge, H.-P., Grand, S.P., 2000. Mesozoic plate-motion history below the northeast Pacific Ocean from seismic images of the subducted Farallon slab. Nature 405, 337–340.

Burgess, P.M., Gurnis, M., Moresi, L., 1997. Formation of sequences in the cratonic interior of North America by interaction between mantle, eustatic, and stratigraphic processes. Geol. Soc. Am. Bull. 108, 1515–1535.

Cagnioncle, A.-M., Parmentier, E.M., Elkins-Tanton, L.T., 2007. Effect of solid flow above a subducting slab on water distribution and melting at convergent plate boundaries. J. Geophys. Res. 112. doi:10.1029/2007JB004934.

Carlson, R.W., Irving, A.J., Schulze, D.J., Hearn Jr., B.C., 2004. Timing of Precambrian melt depletion and Phanerozoic refertilization events in the lithospheric mantle of the Wyoming Craton and adjacent Central Plains orogen. Lithos 77, 453–472.

Choukroun, M., O'Reilly, S.Y., Griffin, W.L., Pearson, N.J., Dawson, J.B., 2005. Hf isotopes of MARID (mica-amphibole-rutile-ilmenite-diopside) rutile trace metasomatic processes in the lithospheric mantle. Geology 33, 45–48.

Comin-Chiaramonti, P., Lucassen, F., Girardi, V.A.V., De Min, A., Gomes, C.B., 2010. Lavas and their mantle xenoliths from intracratonic Eastern Paraguay (South America Platform) and Andean Domain, NW Argentina: a comparative review. Miner. Petrol. 98, 143–165.

Coney, P.J., Reynolds, S.J., 1977. Cordilleran Benioff zones. Nature 270, 403–406.

Cross, T.A., Pilger Jr., R.H., 1978. Tectonic controls of Late Cretaceous sedimentation, Western Interior, USA. Nature 274, 653–657.

Crough, S.T., Morgan, W.J., Hargraves, R.B., 1980. Kimberlites: their relation to mantle hotspots. Earth Planet. Sci. Lett. 50, 260–274.

Cullers, R.L., Dorais, M.J., Berendsen, P., Chaudhuri, S., 1996. Mineralogy and petrology of Cretaceous subsurface lamproite sills, southeastern Kansas USA. Lithos 38, 185–206.

Currie, C.A., Huismans, R.S., Beaumont, C., 2008. Thinning of continental backarc lithosphere by flow-induced gravitational instability. Earth Planet. Sci. Lett. 269, 435–446.

Davies, R.M., O'Reilly, S.Y., Griffin, W.L., 2002. Multiple origins of alluvial diamonds from New South Wales, Australia. Econ. Geol. 97, 109–123.

Davies, R.M., Griffin, W.L., O'Reilly, S.Y., Andrew, A.S., 2003. Unusual mineral inclusions and carbon isotopes of alluvial diamonds from Bingara, eastern Australia. Lithos 69, 51–66.

DeCelles, P.G., 2004. Late Jurassic to Eocene evolution of the Cordilleran thrust belt and foreland basin system, western U.S.A. Am. J. Sci. 304, 105–168.

Dickinson, W.R., Snyder, W.S., 1978. Plate tectonics of the Laramide orogeny. In: Matthews, V. (Ed.), Laramide folding associated with basement block faulting in the western United States: Geol. Soc. Am. Mem., vol. 151, pp. 355–366.

Dimitru, T.A., Gans, P.B., Foster, D.A., Miller, E.L., 1991. Refrigeration of the western Cordilleran lithosphere during Laramide shallow-angle subduction. Geology 19, 1145–1148.

Dixon, J.E., Dixon, T.H., Bell, D.R. Malservisi, 2004. Lateral variation in upper mantle viscosity: role of water. Earth Planet. Sci. Lett. 222, 451–467.

Downes, H., MacDonald, R., Upton, B.G.J., Cox, K.G., Bodinier, J.L., Mason, P.R.D., James, D., Hill, P.G., Hearn Jr., B.C., 2004. Ultramafic xenoliths from the Bearpaw Mountains, Montana, USA: evidence for multiple metasomatic events in the lithospheric mantle beneath the Wyoming Craton. J. Petrol. 45, 1631–1662.

Eccles, D.R., Heaman, L.M., Luth, R.W., Creaser, R.A., 2004. Petrogenesis of the Late Cretaceous northern Alberta kimberlite province. Lithos 76, 435–459.

Eccles, D.R., Heaman, L.M., Sweet, A.R., 2008. Kimberlite-sourced bentonite, its paleoenvironment and implications for the Late Cretaceous K14 kimberlite cluster, northern Alberta. Can. J. Earth Sci. 45, 531–547.

Eiler, J.M., Crawford, A., Elliott, T., Farley, K.A., Valley, J.W., Stolper, E.M., 2000. Oxygen isotope geochemistry of oceanic-arc lavas. J. Petrol. 41, 229–256.

Elliott, T., 2003. Tracers of the slab. In: Eiler, J. (Ed.), Inside the Subduction Factory, Geophysical Monograph Series, vol. 138. American Geophysical Union, Washington DC, pp. 23–45.

Engebretson, D.C., Cox, A., Thompson, G.A., 1984. Correlation of Plate Motions with Continental Tectonics: Laramide to Basin-Range. Tectonics 3, 115–119.

English, J.M., Johnston, S.T., Wang, K., 2003. Thermal modeling of the Laramide orogeny: testing the flat-slab subduction hypothesis. Earth Planet. Sci. Lett. 214, 619–632.

Facer, J., Downes, H., Beard, A., 2009. In situ serpentinization and hydrous fluid metasomatism in spinel dunite xenoliths from the Bearpaw Mountains, Montana, USA. J. Petrol. 50, 1443–1475.

Fullsack, P., 1995. An arbitrary Lagrangian–Eulerian formulation for creeping flows and its application in tectonic models. Geophys. J. Int. 120, 1–23.

Gleason, G.C., Tullis, J., 1995. A flow law for dislocation creep of quartz aggregates determined with the molten salt cell. Tectonophysics 247, 1–23.

Griffin, W.L., Pearson, N.J., Belousova, E., Jackson, S.E., van Achterbergh, E., O'Reilly, S.Y., Shee, S.R., 2000. The Hf isotope composition of cratonic mantle: LAM-MC-ICPMS analysis of zircon megacrysts in kimberlites. Geochim. Cosmochim. Acta 64, 133–147.

Griffin, W.L., O'Reilly, S.Y., Doyle, B.J., Pearson, N.J., Coopersmith, H., Kivi, K., Malkovets, V., Pokhilenko, N., 2004. Lithosphere mapping beneath the North American Plate. Lithos 77, 873–922.

Griffin, W., Stern, R., Leybourne, M., 2009. Episodic Late Cretaceous volcanism in the Balcones Igneous Province, Texas. GSA Abstracts with Programs, vol. 41, p. 14.

Hacker, B.R., 1996. Eclogite formation and the rheology, buoyancy, seismicity, and H_2O content of oceanic crust. In: Bebout, G.E., Scholl, D.W., Kirby, S.H., Platt, J.P. (Eds.), Subduction top to bottom: Geophysical Monograph, vol. 96. American Geophysical Union, Washington DC, pp. 337–346.

Hacker, B.R., 2008. H_2O subduction beyond arcs. Geochem. Geophys. Geosyst. 9, Q03001. doi:10.1029/2007GC001707.

Hacker, B.R., Abers, G.A., Peacock, S.M., 2003. Subduction factory 1. Theoretical mineralogy, densities, seismic wave speeds and H_2O contents. J. Geophys. Res. 108. doi:10.1029/2001JB001127.

Heaman, L.M., Kjarsgaard, B.A., Creaser, R.A., 2003. The timing of kimberlite magmatism in North America: implications for global kimberlite genesis and diamond exploration. Lithos 71, 153–184.

Heaman, L.M., Kjarsgaard, B.A., Creaser, R.A., 2004. The temporal evolution of North American kimberlites. Lithos 76, 377–397.

Helmstaedt, H.H., Gurney, J.J., 1997. Geodynamic controls of kimberlites—what are the roles of hotspot and plate tectonics? Russ. Geol. Geophys. 38, 492–508.

Huismans, R.S., Beaumont, C., 2003. Symmetric and asymmetric lithospheric extension: relative effect of frictional-plastic and viscous strain softening. J. Geophys. Res. 108. doi:10.1029/2002JB002026.

Humphreys, E., Hessler, E., Dueker, K., Farmer, G.L., Erslev, E., Atwater, T., 2003. How Laramide-age hydration of the North American lithosphere by the Farallon slab controlled subsequent activity in the western United States. Int. Geol. Rev. 45, 575–595.

Irving, A.J., Hearn Jr., B.C., 2003. Alkalic Rocks of Montana: Kimberlites, Lamproites and Related Magmatic Rocks, Guidebook Prepared for the VIIIth International Kimberlite Conference, Montana Field Trip 16–21 June 2002. Geological Survey of Canada, Ottawa ON. 44 pp.

Karato, S., Wu, P., 1993. Rheology of the upper mantle: a synthesis. Science 260, 771–778.

Katz, R.F., Spiegelman, M., Langmuir, C.H., 2003. A new parameterization of hydrous mantle melting. Geochm. Geophys. Geosyst. 4. doi:10.1029/2002GC000433.

Kerrick, D.M., Connolly, J.A.D., 2001. Metamorphic devolatilization of subducted oceanic metabasalts: implications for seismicity, arc magmatism and volatile recycling. Earth Planet. Sci. Lett. 189, 19–29.

Le Roex, A.P., Bell, D.R., Davis, P., 2003. Petrogenesis of group I kimberlites from Kimberley, South Africa: evidence from bulk-rock geochemistry. J. Petrol. 44, 2261–2286.

Lee, C.-T.A., 2005. Trace element evidence for hydrous metasomatism at the base of the North American lithosphere and possible association with Laramide low-angle subduction. J. Geol. 113, 673–685.

Li, Z.-X.A., Lee, C.-T.A., Peslier, A.H., Lenardic, A., Mackwell, S.J., 2008. Water contents in mantle xenoliths from the Colorado Plateau and vicinity: implications for the mantle rheology and hydration-induced thinning of continental lithosphere. J. Geophys. Res. 113. doi:10.1029/2007JB005540.

Liu, S., Nummedal, D., 2004. Late Cretaceous subsidence in Wyoming: quantifying the dynamic component. Geology 32, 397–400.

Liu, L., Spasojevic, S., Gurnis, M., 2008. Reconstructing Farallon Plate subduction beneath North America back to the Late Cretaceous. Science 322, 934–938.

Liu, L., Gurnis, M., Seton, M., Saleeby, J., Müller, Jackson, J.M., 2010. The role of oceanic plateau subduction in the Laramide orogeny. Nat. Geosci. 3, 353–357.

Livacarri, R.F., Burke, K., Sengor, A.M.C., 1981. Was the Laramide orogeny related to subduction of an oceanic plateau? Nature 289, 276–278.

Livaccari, R.F., Perry, F.V., 1993. Isotopic evidence for preservation of Cordilleran lithospheric mantle during the Sevier–Laramide orogeny, western United States. Geology 21, 719–722.

Mackwell, S.J., Zimmerman, M.E., Kohlstedt, D.L., 1998. High-temperature deformation of dry diabase with application to tectonics on Venus. J. Geophys. Res. 103, 975–984.

Malkovets, V.G., Griffin, W.L., O'Reilly, S.Y., Wood, B.J., 2007. Diamond, subcalcic garnet, and mantle metasomatism: kimberlite sampling patterns define the link. Geology 35, 339–342.

McCandless, T.E., 1999. Kimberlites: Mantle expressions of deep-seated subduction. In: Gurney, J.J., Gurney, J.L., Pascoe, M.D., Richardson, S.H. (Eds.), Proceedings of the Seventh International Kimberlite Conference, vol. 2, pp. 545–549.

McCandless, T.E., Tosdal, R.M., 2005. Base metal porphyries and diamond-enriched kimberlites of the Laramide orogeny: products of convergent margin magmatism. GSA Abstracts with Programs 37, 97.

Mirnejad, H., Bell, K., 2006. Origin and source evolution of the Leucite Hills lamproites: evidence from Sr–Nd–Pb–O isotopic compositions. J. Petrol. 47, 2463–2489.

Mitchell, R.H., 1986. Kimberlites: Mineralogy, Geochemistry and Petrology. Plenum Press, New York. 442 pp.

Mitrovica, J.X., Beaumont, C., Jarvis, G.T., 1989. Tilting of continental interiors by the dynamical effects of subduction. Tectonics 8, 1079–1094.

Nowell, G.M., Pearson, D.G., Bell, D.R., Carlson, R.W., Smith, C.B., Kempton, P.D., Noble, S.R., 2004. Hf isotope systematics of kimberlites and their megacrysts: new constraints on their source regions. J. Petrol. 45, 1583–1612.

O'Brien, H.E., Irving, A.J., McCallum, I.S., Thirlwall, M.F., 1995. Strontium, neodymium, and lead isotopic evidence for the interaction of post-subduction asthenospheric

potassic mafic magmas of the Highwood Mountains, Montana, USA, with ancient Wyoming craton lithospheric mantle. Geochim. Cosmochim. Acta 59, 4539–4556.
O'Driscoll, L.J., Humphreys, E.D., Sauceri, F., 2009. Subduction adjacent to deep continental roots: enhanced negative pressure in the mantle wedge, mountain building and continental motion. Earth Planet. Sci. Lett. 280, 61–70.
Perkins, G.B., Sharp, Z.D., Selverstone, J., 2006. Oxygen isotope evidence for subduction and rift-related mantle metasomatism beneath the Colorado Plateau–Rio Grande rift transition. Contrib. Mineral. Petrol. 151, 633–650.
Phipps, S.P., 1988. Deep rifts as sources for alkaline intraplate magmatism in eastern North America. Nature 334, 27–31.
Pysklywec, R.N., Beaumont, C., 2004. Intraplate tectonics: feedback between radioactive thermal weakening and crustal deformation driven by mantle lithosphere instabilities. Earth Planet. Sci. Lett. 221, 275–292.
Ringwood, A.E., Kesson, S.E., Hibberson, W., Ware, N., 1992. Origin of kimberlites and related magmas. Earth Planet. Sci. Lett. 113, 521–538.
Rowe, M.C., Lassiter, J.C., 2009. Chlorine enrichment in central Rio Grande Rift basaltic melt inclusions: evidence for subduction modification of the lithospheric mantle. Geology 37, 439–442.
Saleeby, J., 2003. Segmentation of the Laramide slab—evidence from the southern Sierra Nevada region. Geol. Soc. Am. Bull. 115, 655–668.
Schmidt, M.W., Poli, S., 2003. Generation of mobile components during subduction of oceanic crust. Treatise Geochem. 3, 567–591.
Schulze, D.J., Valley, J.R., Bell, D.R., Spicuzza, M.F., 2001. Oxygen isotope variations in Cr-poor megacrysts from kimberlite. Geochim. Cosmochim. Acta 65, 4375–4384.
Sigloch, K., McQuarrie, N., Nolet, G., 2008. Two-stage subduction history under North America inferred from multiple-frequency tomography. Nat. Geosci. 1, 458–462.
Smith, D., 2010. Antigorite peridotite, metaserpentinite, and other inclusions within diatremes on the Colorado Plateau, SW USA: implications for the mantle wedge during low-angle subduction. J. Petrol. 51, 1355–1379.
Smith, D., Griffin, W.L., 2005. Garnetite xenoliths and mantle–water interactions below the Colorado Plateau, southwestern United States. J. Petrol. 46, 1901–1924.
Smith, A.G., Smith, D.G., Funnell, B.M., 1994. Atlas of Mesozoic and Cenozoic Coastlines. Cambridge University Press, New York. 99 pp.
Smith, D., Connelly, J.N., Manser, K., Moser, D.E., Housh, T.B., McDowell, F.W., Mack, L.E., 2004. Evolution of Navajo eclogites and hydration of the mantle wedge below the Colorado Plateau, southwestern United States. Geochem. Geophys. Geosyst. 5. doi:10.1029/2003GC000675.
Spasojevic, S., Liu, L., Gurnis, M., 2009. Adjoint models of mantle convection with seismic, plate motion, and stratigraphic constraints: North America since the Late Cretaceous. Geochem. Geophys. Geosyst. 10. doi:10.1029/2008GC002345.
Stein, C.A., Stein, S., 1992. A model for the global variation in oceanic depth and heat flow with lithospheric age. Nature 359, 123–129.
Sutherland, F.L., Barron, L.M., 2003. Diamonds of multiple origins from New South Wales: further data and discussion. Aust. J. Earth Sci. 50, 975–981.
Thompson, R.N., Velde, D., Leat, P.T., Morrison, M.A., Mitchell, J.G., Dickin, A.P., Gibson, S.A., 1997. Oligocene lamproite containing an Al-poor, T-rich biotite, Middle Park, northwest Colorado, USA. Mineral. Magn. 61, 557–572.
Thomsen, T.B., Schmidt, M.W., 2008. Melting of carbonated pelites at 2.5–5.0 GPa, silicate–carbonatite liquid immiscibility, and potassium–carbon metasomatism of the mantle. Earth Planet. Sci. Lett. 267, 17–31.
Torsvik, T.H., Burke, K., Steinberger, B., Webb, S.J., Ashwal, L.D., 2010. Diamonds sampled by plumes from the core–mantle boundary. Nature 466, 352–355.
Usui, T., Nakamura, E., Kobayashi, K., Maruyama, S., Helmstaedt, H., 2003. Fate of the subducted Farallon plate inferred from eclogite xenoliths in the Colorado Plateau. Geology 31, 589–592.
van der Meer, D.G., Spakman, W., van Hinsbergen, D.J.J., Amaru, M.L., Torsvik, T.H., 2010. Towards absolute plate motions constrained by lower-mantle slab remnants. Nat. Geosci. 3, 36–40.
van Hunen, J., van den Berg, A.P., Vlaar, N.J., 2002. On the role of the subducting oceanic plateaus in the development of shallow flat subduction. Tectonophysics 352, 317–333.
van Hunen, J., van den Berg, A.P., Vlaar, N.J., 2004. Various mechanisms to induce present-day shallow flat subduction and implications for the younger Earth: a numerical parameter study. Phys. Earth Planet. Int. 146, 179–194.
Wannamaker, P.E., Hulen, J.B., Heizler, M.T., 2000. Early Miocene lamproite from the Colorado tectonic province, southeastern Utah, USA. J. Volcanol. Geoth. Res. 96, 175–190.
Warren, C.J., Beaumont, C., Jamieson, R.A., 2008. Deep subduction and rapid exhumation: role of crustal strength and strain weakening in continental subduction and ultrahigh-pressure rock exhumation. Tectonics 27. doi:10.1029/2008TC002292.
Willett, S.D., 1999. Rheological dependence of extension in wedge models of convergent orogens. Tectonophysics 305, 419–435.